

Flow and pollution transport during Wagerup 2006: a case study

Charles Retallack,^{a*} Ron Calhoun,^a H. J. S. Fernando,^a Ken Rayner,^b Anthony Stuart,^b John Sutton^b and Mark F. Hibberd^c

^a *Department of Mechanical and Aerospace Engineering, Arizona State University, Tempe, AZ, USA*

^b *Department of Environment and Conservation, Western Australia, Perth, Australia*

^c *CSIRO, Marine and Atmospheric Research, Aspendale, Australia*

ABSTRACT: As part of a broader field campaign dubbed Wagerup 2006, a case study was carried out to determine the overnight pollution transport mechanisms and flow characteristics near Wagerup, Western Australia. The ambient conditions were characterized by stable stratification with little synoptic influence in the lower boundary layer. An elevated jet intrusion originating on a nearby escarpment slope was found to induce sufficient mixing causing elevated pollution plumes to reach ground level. Onset of mixing was accurately predicted by non-linear critical Richardson number estimates obtained in previous laboratory work. The increase in ground level temperatures brought about by shear induced mixing later prompted a sea-breeze like gravity current that was completely blocked by the escarpment and as a result pollutants were trapped against the escarpment slope. A notable side effect of the topographic blocking was the subsequent steady 360° rotation of ground level winds within an area of influence described by the Rossby deformation radius. Copyright © 2009 Royal Meteorological Society

KEY WORDS pollution transport; stratified flow; shear induced mixing; topographic influences; Doppler lidar

Received 26 February 2009; Revised 10 June 2009; Accepted 11 June 2009

1. Introduction

In light of a proposal by the world's largest aluminium manufacturer, Alcoa Inc., to almost double production at its Western Australian alumina refinery at Wagerup, and given the public concerns about increased industrial production in the proximity of urban areas and past claims that people in the area have suffered health problems related to plant operation, the Department of Environmental Conservation (DEC) of Western Australia, collaboratively with Alcoa Australia, organized a field campaign to map pollutant transport in the Wagerup area. In this multi-group study, dubbed Wagerup 2006, both observations and numerical modelling were conducted to investigate how refinery emissions are transported from point and area sources and mixed to ground level. Other participants of Wagerup 2006 included Arizona State University (ASU), Commonwealth Scientific and Industrial Research Organization (CSIRO), Compliance Monitoring, and Ecowise. The study was particularly focused on assessing the previously proposed pollution pathways and mechanisms.

At Wagerup the effects of terrain and complex atmospheric conditions make the modelling a challenging

task, given that many of the critical dispersion phenomena are sub-mesoscale. The proximity of a 300 m escarpment to the refinery is of special concern with terrain-induced perturbations in stable conditions leading to hydraulic jumps (Pitts and Lyons, 1989), critical layer phenomena, intrusions and jet-like flows, and recirculation regions. The associated inversions may trap the pollutants in the lower layers. Mixing in these regions plays a crucial role in determining the downward diffusion of pollutants to ground level. Two such events were captured in detail in the observations from 28 August 2006 (evening) to 29 August 2006 (morning). The first mechanism involved topographically influenced horizontal transport and down-mixing of pollutants released at various elevations, while the second involved the trapping of elevated pollutants by the topography, allowing buildup of pollutant concentrations aloft. These are the focus of this paper.

The primary goal of the field experiment was to identify atmospheric pollution transport mechanisms specific to the Wagerup area. Since a majority of the air quality complaints are received during winter, presumably due to more stable conditions, the study took place from 7 July to 12 October 2006 (Australian winter). A scanning Doppler lidar was deployed in Wagerup 2006 in order to measure winds and track aerosol plumes emitted from known pollution sources simultaneously. The literature on pollution transport under the influences of atmospheric

* Correspondence to: Charles Retallack, Mechanical and Aerospace Engineering, Arizona State University, Main Campus, PO Box 876106, Tempe, AZ 85287-6106, USA. E-mail: Charles.Retallack@asu.edu

stability and topography is extensive. Lidar has been shown to be advantageous in past industrial atmospheric pollution tracking studies. Eberhard *et al.* (1987) used an aerosol lidar to track power plant emissions over complex terrain. Their lidar results were compared with a ground level sulphur hexafluoride tracer network with good agreement. In another study, an aerosol lidar monitored industrial emissions in the city of Hamilton, Ontario (Pal *et al.*, 1998). This study demonstrated the ability of lidar to track aerosol plumes from multiple industrial sources. Strawbridge (2006) employed an aerosol lidar to track aerosol plumes emitted from a smelter stack. Several fumigation events were detected during the experiment in which the elevated aerosol plume reached ground level. The instruments in each of these experiments were aerosol lidars with the ability to track plumes based on backscatter signal returns. Bozier *et al.* (2007) used a Doppler lidar system to study the effects of convection on the transport of forest fire smoke plumes in the atmospheric boundary layer. The instrument used by Bozier *et al.* (2007) allowed for the detection of aerosol particles as well as radial velocities. The capability of the coherent Doppler lidar deployed in the current experiment to track aerosol plumes and measure radial velocity fields simultaneously was a salient feature of Wagerup 2006, whereby the underlying fluid dynamics responsible for plume transport could be analysed to a high degree of resolution, thus providing a deeper understanding of the atmospheric conditions which led to undesirable plume movements.

Two phenomena are the focus of this paper. The first is the downward mixing of an elevated layer of pollutants through shear-induced mixing at night. A stably stratified boundary layer inhibits the vertical dispersion of pollutants, and upon reaching its layer of neutral buoyancy, a pollution plume may be transported horizontally with little vertical mixing. This elevated layer with a relatively high pollution concentration can be mixed to ground level through convective turbulence or shear induced turbulence. The latter is the active mechanism at night, and is determined by the bulk Richardson number R_b criterion:

$$R_b = \frac{g \left(\Delta\theta / T \right) \Delta z}{(\Delta U)^2 + (\Delta V)^2} \quad (1)$$

where g is gravity, θ is virtual potential temperature, T is absolute temperature, z height, while U and V are horizontal velocities. Although there is no particular R_b criterion available for the breakdown of a stratified shear layer, the linear stability limit for monotonic density and velocity profiles stipulate $R_b < 0.25$ as a necessary condition for instability. The nonlinear stability limit is 1 and the laboratory experiments of Strang and Fernando (2001) showed rapid mixing when $R_b < 1$. Zilitinkevich and Baklanov (2002) have compiled experimentally and numerically determined values for the critical bulk Richardson number with the majority

lying in the 0.2–0.6 range. For the current work, $R_b \sim 1$ is a reasonable estimate for the onset of shear induced turbulence.

The second phenomenon considered in this paper relates to topographic influences on flow and dispersion. As will be discussed later, during the period of interest the synoptic flow is northerly and its interaction with the escarpment appears to be masked by the northeasterly flow from the escarpment, but directional shear appears to be strong and stability of the flow is characterized by (Equation 1). When $R_b < 1$, the breakdown of the stratified layer can carry synoptic flow momentum downward, tending to align the flow with the synoptic flow.

Complicating this event is a sea-breeze-like flow arriving from the southwest. This gravity driven flow undercuts the existing flow. A sea breeze is a mesoscale flow (~ 50 km) with Rossby number $Ro = u/fL \sim 2/(10^{-4} \times 50 \times 10^3) \sim 0.4$, and the Rossby deformation radius of its interaction with the obstacle becomes $L_R = Nh/f \sim 0.01 \times 300/10^{-4} \sim 30$ km, which is larger than the scale of obstacle $L \sim 1.6$ km. Therefore, the local processes of interaction (time scales $T \ll f^{-1}$) can be assumed independent of the rotation, so that they occur in much the same way as that in non-rotating fluids. Since $Nh/U \sim 0.01 \times 300/2 \sim 6$ (> 1) the interaction would produce blocking characterized by a stagnation region with two stagnation points, one at a height of about 0.4 h (a node of attachment) and the other at the foot of the obstacle (saddle point separation) with a weak flow from the former to the latter (Baines, 1995; see figure 6.26, inset). The blocking influence extends to an upstream distance $L \sim 3$ km. At larger times, the blocking would extend to L_R upstream as the rotational adjustment took place (Hunt *et al.*, 2004), but the event does not last long enough for these effects to be observed.

2. Methods

The field campaign studying the local airshed around Wagerup, Western Australia, was carried out from 7 July 2006 to 12 October 2006. Wagerup is located approximately 25 km inland and 100 km south of Perth, Western Australia, near the Darling Scarp. The Darling Scarp is an escarpment that runs roughly north to south near the western coast of Australia. The escarpment rises to a height of approximately 300 m near Wagerup with an approximate half width of 1.6 km (Pitts and Lyons, 1989). Several pollution sources, ranging from ground-level dust aerosols to elevated chimney stacks, are present in the alumina refinery, which is located near the base of the escarpment. Pollutant types and concentrations vary between sources but include CO_2 , CO, NO_x , volatile organic compounds (VOCs), and odours. Of primary concern here are the transport methods of the pollutants to surrounding areas, which was evaluated by deploying several *in situ* and remote atmospheric monitoring devices.

Monitoring sites were dispersed throughout the area in order to obtain a spatially representative meteorological dataset. Figure 1 displays the locations of the main monitoring sites as well as the main chimney stack in relation to the area topography. A scanning coherent Doppler lidar (Lockheed Martin Coherent Technologies) was deployed and operated by Arizona State University at a site west of both the refinery and the escarpment. Meteorological stations were located at Boundary Road, Bancell East, Bancell West, Escarpment and Yarloop. These monitored wind speed and direction as well as air temperature at various heights above ground. The Escarpment and Bancell East meteorological stations were operated by *Ecowise* while the Bancell West station was operated by *Compliance Monitoring*. A flux tower that included a Gill HS Ultrasonic anemometer was deployed at the Boundary Road site. Also located at the Boundary Road site were a Remtech PA0 acoustic sounder, a Vaisala CL31 ceilometer, an Air Quality Monitoring Station (AQMS), and a Proton Transfer Reaction Mass Spectrometer (PTRMS). The ceilometer and acoustic sounder were operated by the DEC and the AQMS by Ecotech, while the remaining devices at the Boundary Road site were operated by CSIRO. Co-located at the Yarloop site were a DEC operated PTRMS and Ecotech operated AQMS. Radiosonde launches were carried out daily at 0700 WST (Western Standard Time = UTC + 8 h) each morning in Wagerup by Alcoa Australia. Unless otherwise noted, all monitoring equipment operated on a continuous 24 h basis with scheduled breaks for calibration and maintenance.

The scanning coherent Doppler lidar uses a 10 cm diameter pulsed infrared laser beam. The 2 mJ laser pulse has a wavelength of 2 μm and pulse rate of 500 Hz. Aerosols in the atmosphere scatter the outgoing laser pulse producing a backscattered signal that is recorded by the lidar. Based on time of travel, Doppler shift compared to outgoing signal, and return signal strength, the device is able to measure radial velocity and a type of

relative aerosol concentration at regular intervals along the laser beam path (Calhoun *et al.*, 2007). In this experiment, data were averaged over 100 pulsed beams yielding 5 Hz data at 88 m intervals along the radial direction of the laser beam. Owing to the dependence of the returned signal on ambient aerosol present in the measurement space, the maximum range of the device varies with ambient conditions. During this experiment, horizontal ranges of 5–6 km were typical: vertical ranges were more limited due to lower aerosol content outside the boundary layer. Scans were performed to obtain a time-varying volumetric dataset of the boundary layer near Wagerup. A combination of Range Height Indicator (RHI) and Plan Position Indicator (PPI) scans were used in repeating patterns, tailored to the scientific questions under investigation. RHI scans yield planes of data perpendicular to the horizontal by scanning at a fixed azimuth angle and varying the elevation angle. PPI scans yield a cone shaped data surface with the cone's axis normal to the horizontal. These scans are performed by holding the elevation angle constant while varying the azimuth angle.

3. Results

In order to characterize specific pollution transport and dispersion mechanisms accurately, the key pieces of information required include meteorology and boundary layer flow structure, as well as measurements of air pollutants and their transport. A combination of pollutant tracking methods and meteorological analysis is used to obtain a picture of possible transport mechanisms.

The coherent Doppler lidar was used to obtain radial wind components and to track pollutant plumes advecting away from source locations in the area. The paths and general shape of aerosol plumes emitted from known sources were derived from collected lidar backscatter data. Based on the geographic location of the lidar and sources of interest, data could be mapped in space along with terrain plots to display source locations and cross-sections of emitted aerosol plumes. The coherent Doppler lidar system used in this study does not possess the means to determine the specific makeup of the aerosols, but as long as the aerosols tracked are representative tracers of the constituent of interest (released from the same source), this distinction is inconsequential with regard to identifying the pathways and dynamical mechanisms responsible for exposures. Support for the use of aerosol backscatter levels to track pathways of (co-emitted) plume constituents is given below in the form of corroboration between backscatter and (ground level) gas analyser data.

Throughout the measurement campaign, pollutants were found to be transported to ground level. Actual modes of transport were varied, depending on weather conditions. Results presented here focus specifically on the evening of 28 August 2006 through to the morning of 29 August 2006.

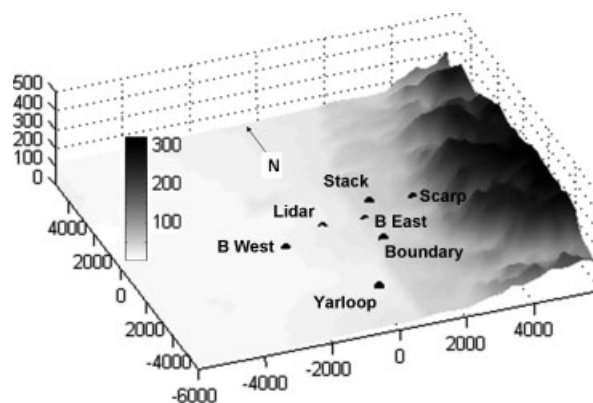


Figure 1. Wagerup 2006 site map. Black dots indicate measurement sites with the exception of 'stack' which indicates the location of the main chimney stack. Bancell East and Bancell West are labelled B East and B West respectively. The escarpment meteorological station is labelled 'scarp' and north is indicated by the arrow. Horizontal distance and vertical elevation are in metres.

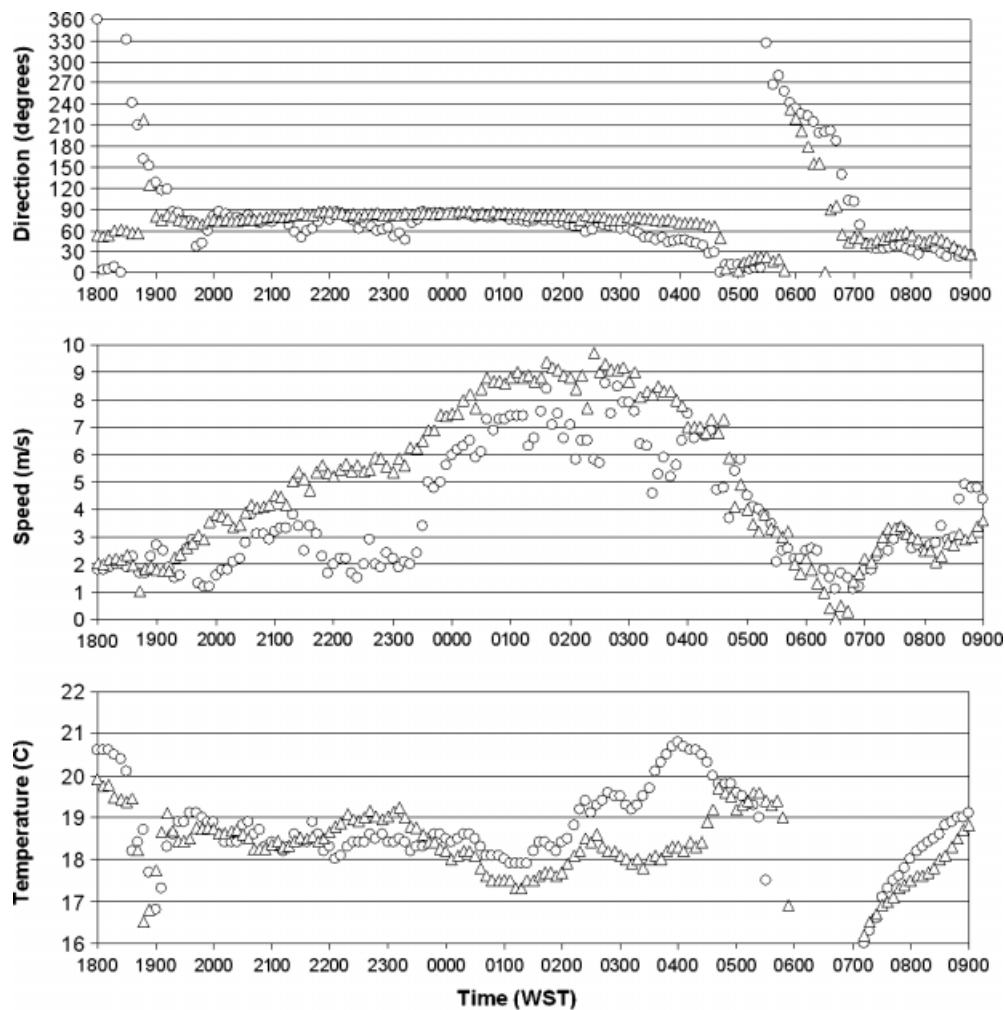


Figure 2. Bancell East 30 m (circles) to Scarp 10 m (triangles) comparison of air temperature along with wind direction and speed for the evening of 28 August 2006 and morning of 29 August 2006. Note that, because of topography, absolute height of Scarp 10 m measurement is 13 m higher than that of Bancell East 30 m.

3.1. Shear-induced mixing event

Before sunset the near surface wind was largely in the direction of the synoptic flow (northerly). After sunset, surface temperatures began to decrease due to radiative losses and ground level winds in the area were very light. At approximately 1900 WST, the wind speed, as measured at the escarpment meteorological station, began to increase and assumed an east-northeasterly direction. The flow resembled a katabatic-type flow descending down the escarpment slope. The velocity of this flow as measured by cup and vane anemometers at the escarpment meteorological station continued to increase in magnitude through midnight with little directional shift. The winds measured by meteorological stations located on the plane below the escarpment were weak (generally $<1 \text{ m s}^{-1}$) with variable directions between east and west through south during this same period. The escarpment site is located at an elevation 33 m above the Bancell East site (Figure 1). Ambient air temperature measurements for the escarpment and data taken at 30 m at Bancell East were in good agreement (Figure 2) and they are notably higher than those measured at

lower levels at measurement sites located on the plane indicating near-surface stable stratification. This shows the development of a shallow pool of cold air on the plane under the downslope flow.

An interesting feature was the inability of the downslope east-northeasterly flow to penetrate this cold surface air mass and upon reaching its neutral density level, the downslope flow left the surface of the slope and continued flowing horizontally over the underlying plane. This behaviour has been noted by Baines (2001) in laboratory work involving density currents flowing down shallow slopes into stably stratified environments and in ocean gravity currents over slopes (Aagaard *et al.*, 1985). Figure 3 shows a lidar RHI velocity plot taken at an azimuth of 285° (looking west). The plot displays an elevated jet-like flow ($\sim 1 \text{ m s}^{-1}$) moving to the west over the plane with a layer of mostly quiescent flow closer to the ground. Due to the stable temperature gradient, the layers were decoupled, allowing the flow from the escarpment to accelerate over the plane with little disturbance to the layer below. During this period, that lasts until just before midnight, the main pollutant plumes (elevated

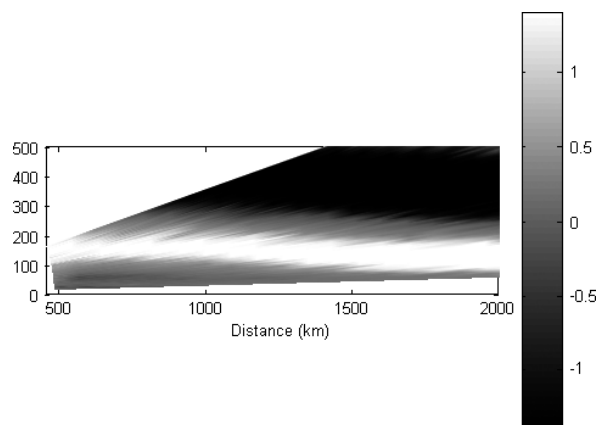


Figure 3. Lidar velocity plot displaying elevated jet like easterly flow. The scale on the right represents wind velocity in m s^{-1} with positive velocity being radially away from the lidar. The jet is seen here between 100 and 200 m above ground and is represented by the white region bounded above and below by darker regions. The plot represents an RHI scan taken at an azimuth angle of 284.9° clockwise from north at 2002 WST on 28 August 2006.

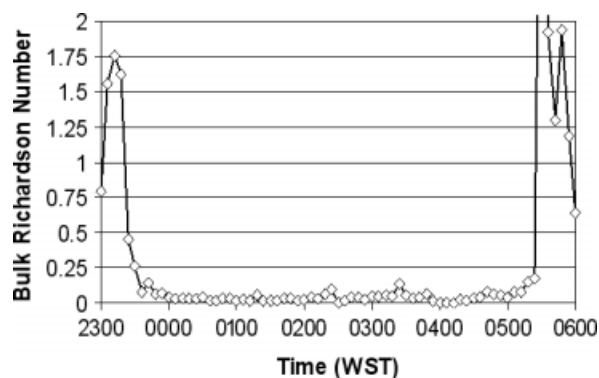


Figure 4. Bulk Richardson number calculated from Bancell East data. The bulk Richardson number is shown to be below critical value for the mixing period between midnight and 0500 WST on 29 August 2006.

sources) were advected down wind (to the west) above the surface layer.

The easterly escarpment flow continued to accelerate (to about 8 m s^{-1} by midnight), increasing the amount of shear between the escarpment flow layer and the dense air layer at ground level. Momentum from this flow also slowly diffused downward, creating shear in the layer below. Just before midnight, the bulk Richardson number calculated based on the lower layer data from Bancell East began to decrease below the critical level of $R_b \sim 1$. Figure 4 shows that the Richardson number remained sub-critical throughout the early morning. Reynolds stresses measured at the flux tower site, shown in Figure 5, displayed turbulent mixing occurring at lower levels during this period of sub-critical bulk Richardson number. The two periods, where the Reynolds stresses indicated mixing and where the Richardson number became sub-critical, coincide and this mixing continues between midnight and 0500 WST on 29 August. The wind vectors at most of the surface sites on the plane also

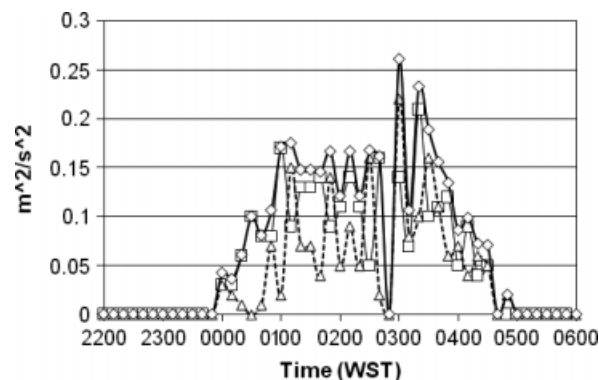


Figure 5. Reynolds Stress retrieved from Flux Tower data at the Boundary Road measurement site. Measurements were taken at 2.8 m height above ground. The square with thin line represent $u'w'$; the triangle with dashed line represents $v'w'$; the diamond with thick line represents the RMS value. Here evidence of turbulent mixing is captured between midnight and 0500 WST on 29 August 2006.

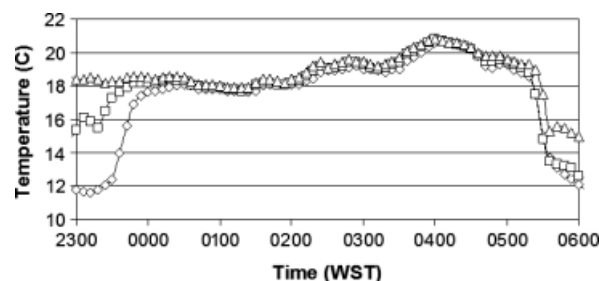


Figure 6. Bancell East temperature traces displaying the destruction of the ground level stratification represented by the collapsing of the temperature traces between 2300 WST and midnight on 28 August 2006. Measurements were taken at 2 m (diamonds), 10 m (squares), and 30 m (triangles) above ground level.

swung into alignment with the downslope flow. Additionally, ambient air temperature traces retrieved at Bancell East at heights of 2, 10 and 30 m above ground level, which lies below the level of the jet, show an isothermal layer coinciding with the original 30 m level temperature, thus indicating the downward transport of warmer air from levels above 30 m (Figure 6). This warming of underlying boundary layer air due to shear-induced turbulence has been observed in previous studies including that of Mahrt (1985) and Pardyjak *et al.* (2002). Figure 7 shows the downward mixing caused by the elevated jet results in an easterly flow at ground level. The pollutant plumes that were previously being advected aloft were, during the turbulent downward mixing period, found to reach ground level. Figure 8 is a lidar backscatter RHI plot taken at 75° azimuth. The lighter regions represent areas of high backscatter and, thus, high aerosol levels. The aerosol plumes can be traced back to sources in the industrial area. The pollutant plumes were moving to the west and rapidly reaching ground level.

The period of turbulent mixing began to subside around 0500 on 29 August. The wind direction as measured at the ground level sites began to shift to a northerly direction with decreasing velocity. The pollutant plume is also shifted and began travelling towards the south.

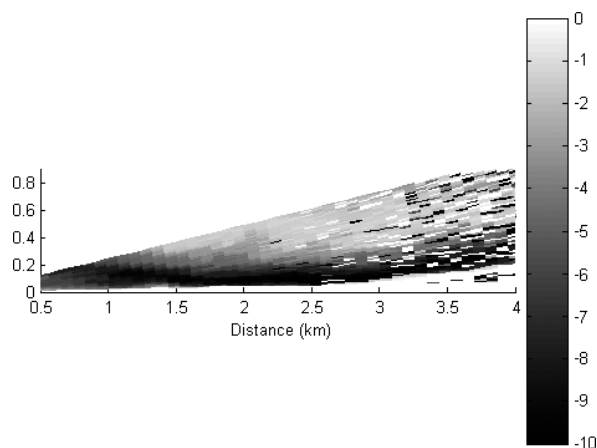


Figure 7. Lidar RHI plot showing easterly elevated jet flow momentum mixed to ground level creating an easterly flow on lower plane. The plot represents lidar velocity data with velocity scale at right of plot given in m s^{-1} . The black region represents flow from east to west leaving the escarpment and moving towards the lidar. The RHI was taken at 90° clockwise from north at 0004 WST on 29 August 2006.

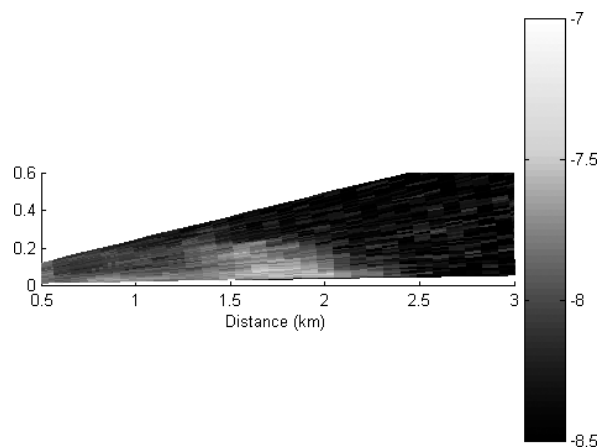


Figure 9. Lidar RHI Backscatter plot showing cross-section of southward propagating pollutant plume (light region). High backscatter returns are shown at measurement angle in closest possible proximity to the ground. The plot represents an RHI scan with azimuth angle of approximately 135° clockwise from north taken at 0506 WST on 29 August 2006. The right hand scale represents backscatter with lower absolute value representing higher aerosol concentration.

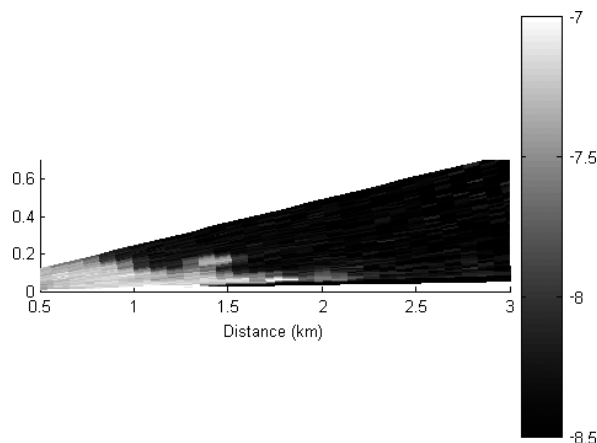


Figure 8. Lidar RHI backscatter plot showing ground level plume in light region, emanating from the area of interest and moving from east to west towards the lidar unit. The plot represents an RHI scan with azimuth angle of approximately 75° clockwise from north taken at 0124 WST on 29 August 2006. The scale on the right is backscatter (arbitrary units) with lower absolute value representing higher aerosol concentration.

Figure 9 is a lidar backscatter RHI plot displaying a cross-section of this plume at 0506 WST. The plotted surface is roughly perpendicular to the pollutant plume's direction of travel and shows the plume was still near ground level. Figure 10 is a 2.5° elevation angle PPI lidar backscatter plot showing the horizontal propagation of the pollutant plume. This figure displays the bulk of the pollutant plume emanating from known sources represented by the white spots located 0.5 km north and 1.5–2 km east of the lidar. In Figure 10, the location of the RHI transect shown in Figure 9 is represented by the diagonal line between the origin and the 1.5 km mark on the abscissa. The lowest elevation angle that Figure 9 includes is 1.1° from horizontal. Obtaining data at lower angles closer to the horizontal was not possible at this azimuthal angle due to ground clutter. Data collected at

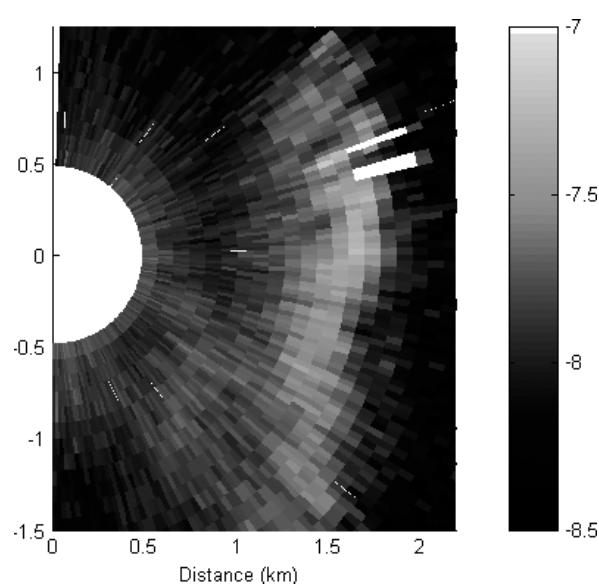


Figure 10. Lidar PPI Backscatter plot showing southward propagating plume in lighter region originating from known sources represented by white blocks at approximately 0.5 km north and 1.7 km east of the lidar. The diagonal line connecting the origin to the 1.5 km x -axis mark represents the location of the RHI shown in Figure 9. The plot represents a PPI scan of elevation angle 2.5° retrieved at 0509 WST on 29 August. The scale is as described in Figure 9.

the 1.1° level in this plot shows the highest backscatter value (indicating high aerosol levels) is located at approximately 1750 m horizontally from the lidar at a bearing of 135° clockwise from north. At this location, the lowest lidar backscatter data measured was approximately 18 m above ground-level. The combination of the close proximity of high aerosol levels to the ground and the traceability of its plume to a known industrial source is strong evidence of an undesirable pollution pathway towards Yarloop township.

Additional evidence strengthens the interpretation above. NO_x is a byproduct of calcination and power

generation processes in the area (CSIRO, 2004). The byproducts of these processes are released from chimney stacks at heights ranging from 40 to 100 m above ground level. NO_x concentrations measured near ground level, below the location of the pollutant plume displayed in the previous lidar backscatter plot, were compared in time to the lidar data. As the ground level wind direction shifted from easterly to northerly the pollutant plume also shifted directions. During this time, the pollutant plume swept over the location of the NO_x sensor (at the Boundary Rd site), whose measurement signal can be seen in Figure 11. The figure shows a marked increase in NO_x just after 0500 WST when the pollutant plume begins to pass over the area (corresponding to a wind direction of about 10°). This suggests that the pollutant plume displayed in the lidar backscatter data is indeed reaching ground level. Similar corroborating evidence is not available during the period between midnight and 0500 WST, since the pollutant plume was moving away (westward) from the NO_x sensor. It is noted that uncertainties arise in using NO_x as an indicator of the presence of ground level plumes because there are other possible sources of NO_x including automobile traffic on the nearby highway, railway activity in the area and domestic heating.

In the period of turbulent mixing after midnight, warm (less dense) air was mixed with a layer of lower-lying cold (denser) air. A plot of ambient air density from data taken at the flux tower (Figure 12) shows the resulting lowered air density that persisted throughout the duration of the turbulent mixing period.

3.2. Pollution trapping event

Coinciding with the end of the mixing event at 0500 WST, measurements taken at all of the meteorological stations show a rapid decrease in temperature coupled with an increase in relative and absolute humidity. Figure 13 shows that these temperature decreases occurred with a time lag between measurement sites. The sites also all show a 360° counterclockwise rotation of the wind over the next couple of hours. This

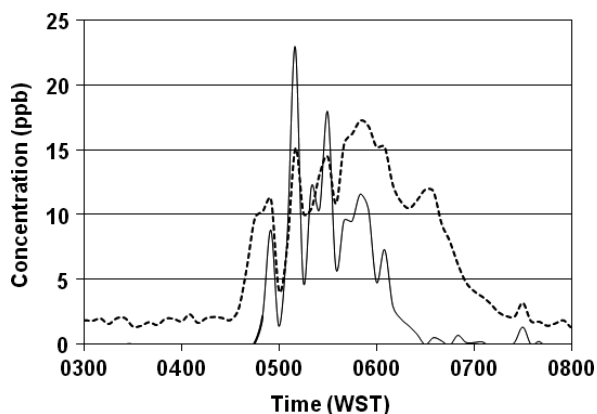


Figure 11. NO_x traces from AQMS showing increased signatures after 0500 WST on 29 August 2006. The solid line represents NO; the dashed line represents NO_2 .

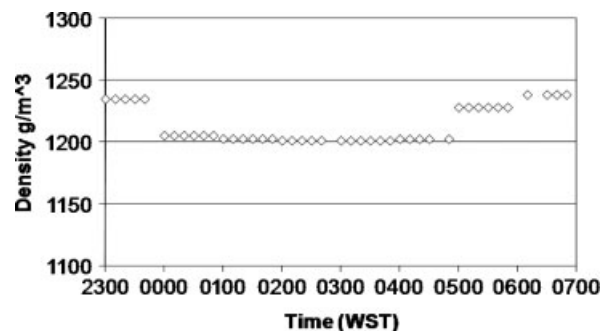


Figure 12. Air density retrieved from Flux Tower data at Boundary Road site. The decrease in density associated with the turbulent mixing period and subsequent increase in density brought on by the sea-breeze-like front are displayed. Data were taken at 2.8 m height above ground.

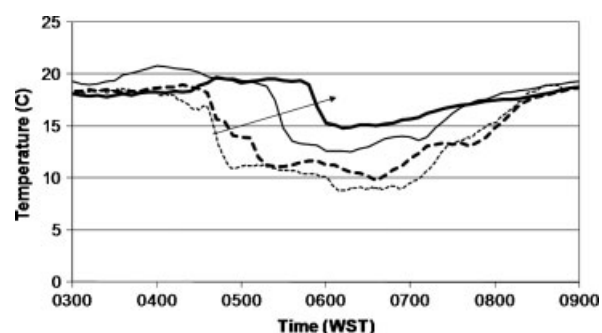


Figure 13. Temperature traces showing sea-breeze-like front propagation and arrival at each of the measurement sites. Temperature is measured at approximately 10 m above ground level at each measurement site. The thin dashed line is Yarloop; the thick dashed line is Bancel West; the thin solid line is Bancel East; the thick solid line is Escarpment. The time lag between abrupt temperature drops suggests a west to east propagation represented by the arrow.

may have been caused by a sea-breeze-like front moving into the area from the west southwest. Simpson *et al.* (1977) used a measured increase in dew point coupled with a change in wind direction as an indication of the arrival of a sea-breeze front. As relative humidity increases the dewpoint also increases, allowing for a measured increase in relative humidity to be used in a similar manner (Lawrence, 2005). The progression of this sea-breeze-like front is displayed by the arrow in Figure 13, which indicates that the temperature decreases progress from west to east and from a lower elevation to higher elevation. It is possible to evaluate the speed of the sea-breeze current as $U_{sb} \sim k(g\Delta T h_{sb}/T_{bar})^{1/2}$ with $\Delta T \sim 10$ K, $T_{bar} \sim 288$ K (Figure 13), and $k \sim 1$ (Simpson, 1997). By taking the thickness of the sea-breeze as 50 m (from lidar records), it is possible to evaluate $U_{sb} \sim 4$ m s^{-1} , and this agrees well with the speed of the front that arrived at ~ 0500 WST (Figure 14). Although sea-breezes are typically a daytime phenomenon caused by density gradients brought on by radiative heating of the onshore air mass, a warm mass of ground-level air created by turbulent mixing described above could also prompt such a flow when in proximity to the sea.

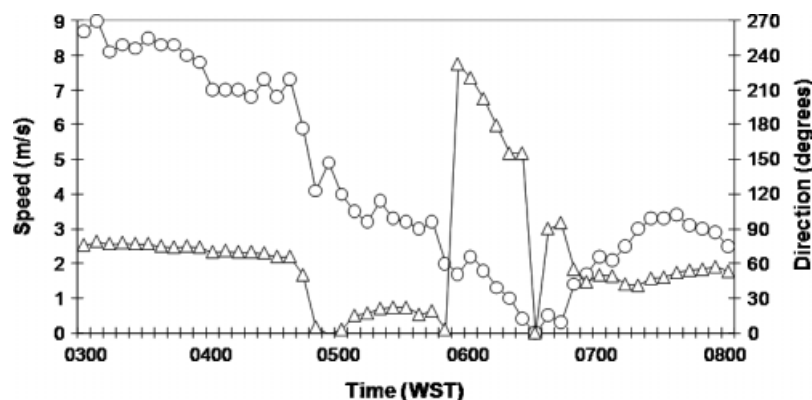


Figure 14. Escarpment wind speed (circles) and wind direction (triangles) data showing stagnation of the impinging flow on the escarpment that takes place at 0630 WST on 29 August 2006. Measurements taken at 10 m above ground level with wind direction given in degrees clockwise from north.

The sea breeze-like density current began to impinge on the escarpment and a stagnation point was reached at around 0630 WST at the escarpment station. This is shown in Figure 14 by the wind speed which slowed to zero at this time, followed later by rapidly increasing winds. As discussed in Section 2, the Nh/U value during the impingement was about 6, and thus the local flow behaviour ought to be similar to that of Figure 15 during the period of westerly to southwesterly winds. Two stagnation regions are expected with weak flow from the higher one to the lower one. The stagnation is clear from the velocity taken by the scarp site at 10 m. Additionally, the scarp temperature reached a minimum at the point of this stagnation before increasing again as the cold air mass receded. The flow reversal seen during stagnation is in good agreement with previous

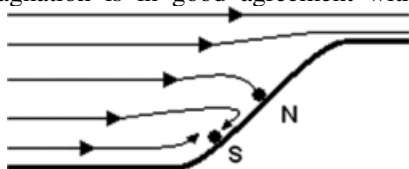


Figure 15. The impingement of a stratified flow on a three dimensional object, when $Nh/U > 1$ (Baines, 1995). The attachment node is the marker labelled N while the saddle point is labelled S. Note the flow reversal.

research reported by Baines (1995), as indicated in Figure 15 for cases $Nh/U > 1$. This reversal of wind (as seen in Figure 16) was measured independently at the various meteorological stations in the area, but the actual spatial extent was only realized through analysis of the Doppler lidar data. A series of lidar PPI velocity plots captures the spatial extent and temporal evolution of the shallow layer wind rotation (Figure 17). On a broader spatial swath, the wind direction change can be inferred by considering the data in Figure 17 within the first 1.5 km radial distance from the origin (within the black circle of Figure 17(a)) – this corresponds to depths up to 65 m. Note the coupled dark to light patches progressing from plot (a) to (f). The dark shading represents negative velocity (radially towards the lidar) and the light shading represents positive velocity (radially away from the lidar). Thus, in the 1.5 km radial range, close to the ground, Figure 17(a) shows a westerly wind direction, Figure 17(c) shows a southerly wind direction, and Figure 17(e) shows an easterly wind direction. The dynamics of the sloshing motions can be explained by the phenomenon of blocking at the escarpment. While the blocking taking place over 1 h is a local phenomenon, as discussed in Section 2, the influence propagates with time over the Rossby deformation radius. Previous studies have shown that once blocking occurs over a larger

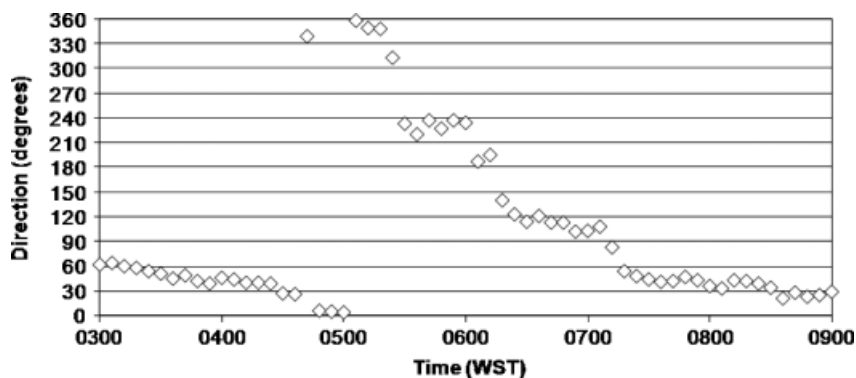


Figure 16. Bancell East 10 m wind direction plot showing 360° rotation of wind direction between approximately 0500 and 0700 WST on 29 August 2006. Wind direction is given in degrees clockwise from north.

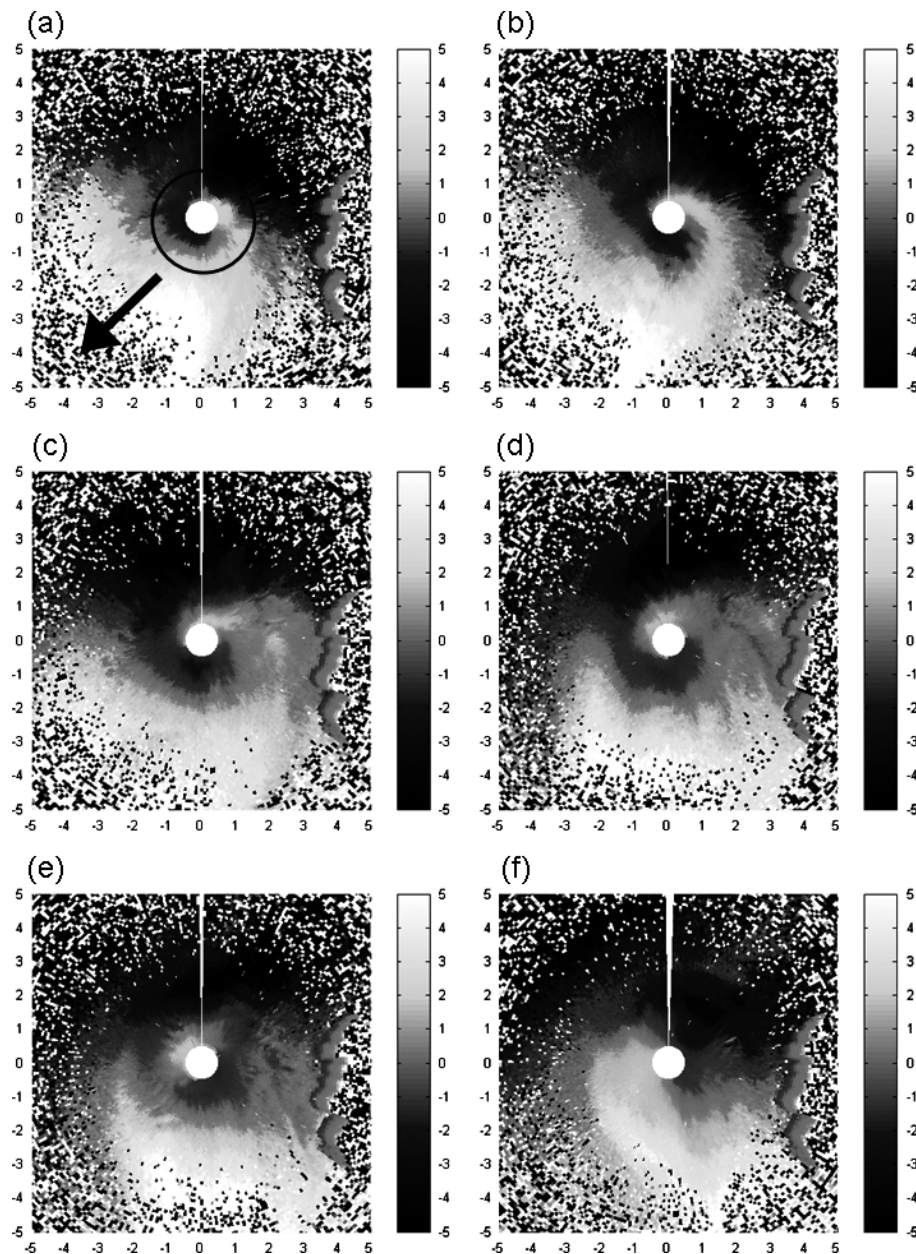


Figure 17. Lidar 2.5° PPI wind velocity plots showing rotation of shallow flow layer on 29 August 2006. The distance scales are in kilometres while the velocity scale is 5 to -5 m s^{-1} radial with respect to the lidar. The positive y-axis is north. The lidar is located at the origin of the plot while the escarpment can be seen here as the stationary jagged data return near the 4 km east of the origin in each plot. The arrow in (a) represents the direction of the synoptic wind, while the black circle in (a) represents a radial distance of approximately 1.5 km from the lidar. (a) At 0527 WST, the shallow flow is seen here in the first 1 km radially from the centre of the plot and is from the west. The flow at higher elevation is northerly. (b) At 0548 WST, the shallow flow begins to assume a southwesterly direction. The upper level flow is relatively unchanged. (c) By 0618 WST, the shallow flow layer is now from the south while the higher elevation flow continues to be northerly. (d) At 0639 WST, the shallow layer flow is southeasterly. (e) At 0649 WST, the shallow layer flow is easterly, moving away from the escarpment. Again the higher elevation flow is mostly unchanged and from the north. (f) By 0709 WST, the shallow layer flow has rotated to a northeasterly direction and begins to align with the direction of the flow aloft.

scale, a flow should be deflected to the right around the obstacle for the southern hemisphere (Pierrehumbert and Wyman, 1985; Overland and Bond, 1995; Thorsteinsson and Sigurdsson, 1996). The significance of blocking with regard to pollution transport stems from the fact that the impinging density current undercut the layer occupied by the aerosol pollutants. These pollutants are then redirected towards the escarpment where they became trapped against the topography and are transported down

slowly. This leads to a possible fumigation during the morning transition period, making this a particularly undesirable development.

4. Conclusion

The presented study highlights the difficulties involved in identifying potential dispersion phenomena in the presence of complex atmospheric conditions and terrain.

This particular case study involved flow patterns evolving in relatively short times but possessing the ability to greatly alter the dispersion characteristics of pollutant plumes in the area. Using an array of remote and *in situ* measurement devices allowed pollutant transport pathways to be linked to the prevailing atmospheric conditions. Of prime importance was the ability of the scanning coherent Doppler lidar to measure aerosol plumes coupled with radial velocities over a wide area.

The atmospheric conditions occurring during the present case study, including elevated jet-induced down-mixing, the penetration of a sea breeze-like air mass, the blocking of this air mass by local topography and a subsequent 360° rotation of lower-level winds, demonstrates the immense complexity of flows involving stable stratification and topography. Each of the observed atmospheric events created unique dispersion conditions increasing the desire for the ability to track the emitted pollutant plumes which typically remain visible for only a few hundred metres downwind once they have entered the atmosphere. Coherent Doppler lidar proves to be a valuable tool for monitoring such events due to both its ability to measure flow fields and aerosols in the boundary layer. As has been shown, the ability to track aerosol plumes from their sources to downwind measurement sites removes some of the ambiguity that can be associated with *in situ* measurement analysis and ultimately provides a better understanding of the overall transport and dispersion characteristics.

Acknowledgements

The ASU lidar group gratefully acknowledges funding for this research from the Western Australian Department of Environment and Conservation (sponsor award number is 06-126406), and also for Army Research Office funding (grant W911NF-04-1-0146, Project Officer: W. Bach) which allowed development of analytical and processing tools. We would also like to thank CSIRO and Alcoa Australia for their respective roles in the collaborative measurement campaign.

References

Aggaard K, Swift JH, Carmack EC. 1985. Thermohaline circulation in the Arctic Mediterranean seas. *Journal of Geophysical Research* **90**: 4833–4846.

- Baines PG. 1995. *Topographic Effects in Stratified Flows*. Cambridge University Press: Cambridge, 482.
- Baines PG. 2001. Mixing in flows down gentle slopes into stratified environments. *Journal of Fluid Mechanics* **443**: 237–270.
- Bozier KE, Pearson GN, Collier CG. 2007. Doppler lidar observations of Russian forest fire plumes over Helsinki. *Weather* **62**: 203–208.
- Calhoun R, Princevac M, Fernando H. 2007. Atmospheric measurements. In *Springer Handbook of Experimental Fluid Mechanics*, Tropea C, Yarin A, Foss JF (eds). Springer: Berlin; 1157–1178.
- CSIRO. 2004. Wagerup air quality review, <http://www.epa.wa.gov.au/docs/1215/response/appc.pdf> (accessed 22 October 2008).
- Eberhard WL, McNice GT, Troxel SW. 1987. Lidar sensing of plume dispersion: analysis methods and product quality for light-scattering tracer particles. *Journal of Atmospheric and Oceanic Technology* **4**: 674–689.
- Hunt JCR, Orr A, Rottman JW, Capo R. 2004. Coriolis effects in mesoscale flows with sharp changes in surface conditions. *Quarterly Journal of the Royal Meteorological Society* **130**: 2703–2731.
- Lawrence MG. 2005. The Relationship between relative humidity and the dewpoint temperature in moist air: a simple conversion and applications. *Bulletin of the American Meteorological Society* **86**: 225–233.
- Mahrt L. 1985. Vertical structure and turbulence in the very stable boundary layer. *Journal of the Atmospheric Sciences* **42**: 2333–2349.
- Overland JE, Bond NA. 1995. Observations and scale analysis of coastal wind jets. *Monthly Weather Review* **123**: 2934–2941.
- Pal SR, Hlaing D, Carswell AI, Roy G, Bastille C. 1998. Scanning lidar application for pollutant sources in an industrial complex. *Proceedings of SPIE-The International Society for Optical Engineering* **3504**: 16–86.
- Pardyjak ER, Monti P, Fernando HJS. 2002. Flux Richardson number measurements in stable atmospheric shear flows. *Journal of Fluid Mechanics* **459**: 307–316.
- Pierrehumbert RT, Wyman B. 1985. Upstream effects of mesoscale mountains. *Journal of the Atmospheric Sciences* **42**: 977–1003.
- Pitts RO, Lyons TJ. 1989. Airflow over a two-dimensional escarpment. I: observations. *Quarterly Journal of the Royal Meteorological Society* **115**: 965–981.
- Simpson JE. 1997. *Gravity Currents in the Environment and the Laboratory*. Cambridge University Press: Cambridge, 258.
- Simpson JE, Mansfield DA, Milford JR. 1977. Inland penetration of sea-breeze fronts. *Quarterly Journal of the Royal Meteorological Society* **103**: 47–76.
- Strang EJ, Fernando HJS. 2001. Entrainment and mixing in stratified shear flows. *Journal of Fluid Mechanics* **428**: 349–386.
- Strawbridge KB. 2006. Scanning lidar: a means of characterizing the Noranda-Horne smelter plume. *Geochemistry: Exploration, Environment, Analysis* **6**: 121–129.
- Thorsteinsson S, Sigurdsson S. 1996. Orographic blocking and deflection of stratified air flow on an f-plane. *Tellus* **48A**: 572–583.
- Zilitinkevich S, Baklanov A. 2002. Calculation of the height of the stable boundary layer in practical applications. *Boundary Layer Meteorology* **105**: 389–409.